# Chapter 3
# Alignment and Calibration of the CMS Tracker

This chapter describes the calibration of the CMS tracker, and in particular its alignment [1–3]—the position, orientation, and shape of each of its modules as recorded in the CMS reconstruction software. The alignment is a crucial ingredient in translating the information provided directly from the tracker readout, the position of each hit relative to the module, to the information we actually want, the hit's location in 3D space.

For the pixel modules, the precision of a hit measurement is typically a few microns. Therefore, we need to know the module's location to similar precision. This is much smaller than errors that can be introduced when building the detector. In addition, the modules tend to move over time, in particular when the magnetic field is turned on or off or when the temperature changes. Therefore, a regular database-based *alignment* is needed to maintain the precision of the detector. Some changes only cause the large mechanical structures to move; for example, the two halves of BPIX and two halves of each endcap of FPIX are especially sensitive to magnetic field changes. In those cases, only those structures may need to be aligned. The detector is designed in a hierarchy of structures, shown in Fig. 3.1, any of which can be aligned while keeping the relative positions of its components fixed.

Tracker alignment is not like a tire alignment. A tire alignment involves the mechanic jacking up the car and physically moving its wheels to their correct positions and orientations. By contrast, when we align the tracker, we do not go down to the CMS cavern and move any modules, because whether the module positions exactly match the design specifications is not the point. What matters is that the module positions assumed in the track reconstruction match the actual positions of the modules. Alignment can be done months or even years after data taking, and the data can be reconstructed with the new alignment.

On the other hand, it is important that the detector not be *too* misaligned at the time of data taking, because this can affect the track information that goes into the high level trigger. While events that pass the trigger can always be rereconstructed later, events that fail the trigger are lost forever. This happened at the beginning of
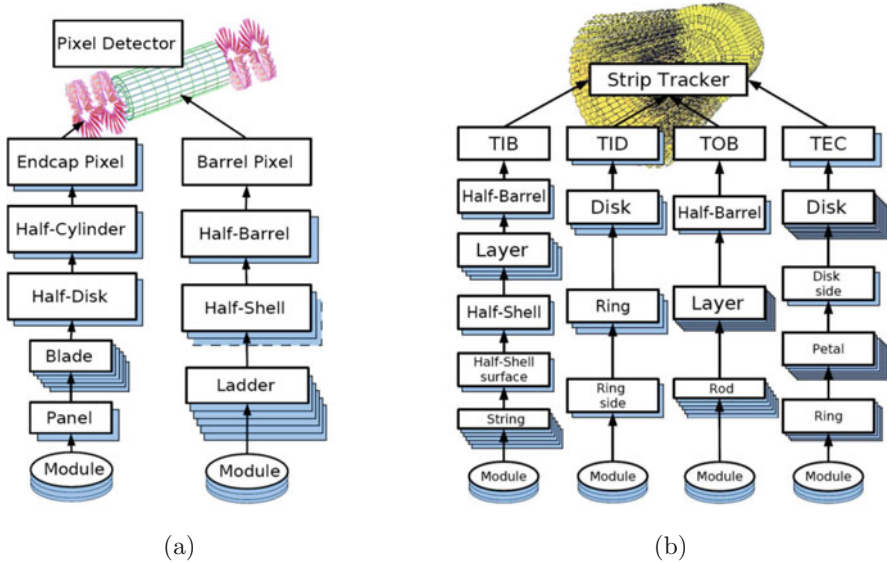
(a)                                                                        (b)

**Fig. 3.1** Hierarchies of the pixel (**a**) and strip (**b**) components of the tracker. Any of these levels of the hierarchy can be aligned [1]

the 2015 run, after the detector had been shut down for 2 years. The first cosmic ray data revealed that one side of FPIX was several millimeters away from its assumed position, as shown later in Fig. 3.17a, and as a result the rate of tracks in that side of FPIX was around 50% of the rate in the other side. Many of the events with lost tracks were triggered due to information in the muon systems, but the tracks were not reconstructed by the software because the misalignment was severe enough to ruin the pattern recognition responsible for track finding. those events could be recovered by first performing a rough alignment with the tracks that were not rejected and then rereconstructing the data using the new geometry, matching the individual hits to form a track. Any events that did *not* pass the muon trigger were just gone. Such a large error would probably not happen during the more crucial collision data taking, but a severe enough miscalibration could result in the loss of important events.

The alignment procedure can be done at a hierarchical level: it is possible, for instance, to align large structures while keeping the individual modules attached to those structures fixed. Typically, while CMS is running, an automatic procedure aligns the six pixel structures: two half barrels of BPIX and two half cylinders on each side of FPIX. This procedure, with only 36 degrees of freedom, is simple enough to run without human input. Every few weeks, an alignment of the pixel modules is performed manually. At the end of the year, with the increased statistics of the full year's data, a new alignment is derived covering the entire year. The strips, which are known to be fairly stable and where small movements have less of an impact on track resolution, are typically only aligned at the beginning of the run period and during this full-year alignment.

## 3.1 Principles of Detector Alignment

The alignment is performed using the data collected. A simple example is shown in Fig. 3.2. When a track is reconstructed with a misaligned geometry, the result is as shown on the right side of the illustration. The expected positions of the hits, calculated from the track's path and shown in red, and the measured hits, shown in green, no longer match. This indicates that the detector is misaligned: its assumed position is wrong.

A real alignment involves many more modules, up to all 17004 (since 2017; the number of modules was previously slightly smaller) for the most comprehensive cases. The assumed positions of any of these modules could be wrong, and we need to fit for all of their positions and rotations in three dimensions. For each module, a local coordinate system is used, as shown in Fig. 3.3. The $w$ axis is perpendicular to the module, and the $u$ and $v$ axes are within it, with the $u$ axis in the more sensitive

**Actual position**             **Assumed position**

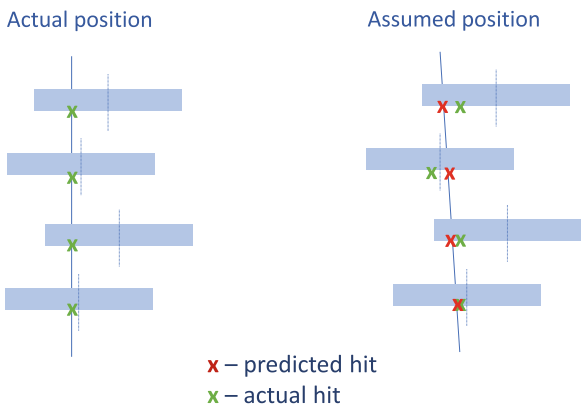x – predicted hit
x – actual hit

**Fig. 3.2** A simplified illustration of how alignment works. The left side shows the actual position of the detector at the time of data taking, with a blue track, taken with the magnetic field turned off, that leaves four hits shown in green. The right side shows the assumed detector position, with the second module from the top assumed to be slightly to the left of its actual position, with the same measured hits in green and the expected hits in red
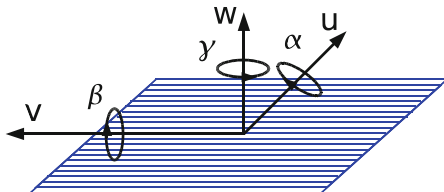
**Fig. 3.3** Illustration [2] of the module local coordinates $u$, $v$, $w$ and the corresponding rotations $\alpha$, $\beta$, $\gamma$ for a module. Three other alignment parameters, not shown here, define the curvature of the module

direction of measurement. The angles $\alpha$, $\beta$, and $\gamma$ describe rotations around $u$, $v$, $w$ respectively.

Millions of tracks are used simultaneously for a more precise measurement of all of the module positions. The magnetic field is turned on and the tracks have curvature. Unlike the exact hit positions shown in the picture, the hit measurements have an intrinsic uncertainty, as do the expected hit positions, which are calculated from the other hits on the track. Additionally, the track parameters themselves are affected by the alignment, so a procedure is needed to deal with those correlations as well.

The alignment parameterization in CMS also includes three degrees of freedom for the deformation of the modules, expanding the curved shape of the modules up to quadratic terms: $\Delta w = s_u u^2 + s_v v^2 + s_{uv} uv$. In general, these deformations are determined by the mechanical stresses on the modules and tend not to change over time, so they are aligned infrequently.

## 3.2  Alignment Algorithms

Two algorithms are used on CMS to perform this minimization and determine alignments: MillePede and HipPy. The ultimate goal is to minimize the objective $\chi^2$ function:

$$\chi^2(\vec{p}, \vec{q}) = \sum_j^{\text{tracks}} \sum_i^{\text{hits}} \left( \frac{m_{ij} - f_{ij}\left(\vec{p}, \vec{q}_j\right)}{\sigma_{ij}} \right)^2 \tag{3.1}$$

where $m_{ij} \pm \sigma_{ij}$ is the measured position of each hit and $f_{ij}$ is the expected position, which depends on the positions, rotations, and deformations of the modules $\vec{p}$ and the track parameters $\vec{q}_j$. (In the case of the pixels, $\vec{f}_{ij}$ and $\vec{m}_{ij} \pm \vec{\sigma}_{ij}$ are two-dimensional vectors with components in the $u$ and the $v$ direction.) We minimize this $\chi^2$ with respect to $\vec{p}$ and $\vec{q}_j$, with the primary goal being $\vec{p}$. Both algorithms start by linearizing $f_{ij}$, and any nonlinear parts are handled by running iterations. The quantity in the numerator of Eq. (3.1) is the difference between the measured hit and the reconstructed hit and is known as the *residual*. If, as is typically the case, $f_{ij}$ is calculated only using $m_{i'j}$ for $i' \neq i$, then the residual is *unbiased*, because $m_{ij}$ and $f_{ij}$ are independent. The residuals in Fig. 3.2, on the other hand, are biased, because a single track is calculated from all of the green hits $m_{ij}$, and that track is used to predict the red hits $f_{ij}$.

It should be stressed that alignment is not just a mathematical problem of minimizing Eq. (3.1). Certain degrees of freedom are not well-constrained by the tracks. Those degrees of freedom are known as weak modes, and some of them will be described in Sect. 3.4. While in theory alignment should never make the situation worse, in practice there can be biases in track reconstruction that lead to false shifts in position. Sometimes this can be useful, as alignment can smooth over effective

shifts and recover degraded performance, but in other situations, particularly when the bias causes movement along a degree of freedom that is weakly constrained, this can make the bias in data worse. An example of this will be shown in Sect. 3.4.1.1, where an unknown bias causes a tension between positively and negatively charged collision tracks, with the result that the alignment gets significantly worse in an attempt to compromise between them. Extra constraints need to be added into the procedure to prevent this.

### 3.2.1  MillePede

The MillePede algorithm [4, 5] does a simultaneous fit for $p_i$ as well as $q_j$, automatically resolving most of the correlations between track parameters and alignment parameters. The size of the linearized $\chi^2$ matrix is the number of module parameters, $17004 \times 6 \approx 10^5$ for a full scale alignment, plus the number of track parameters, which could be $10^7$. However, most of the matrix's entries are 0: the parameters of one track only have direct correlations with the modules hit by that track. This fact allows MillePede to reduce the matrix to a more reasonable $10^5 \times 10^5$ matrix.

In order to improve the computation speed, the MillePede fit runs outside the CMS software package using independent Fortran code. The track propagation model is similar, but not identical, to the standard CMS model. This is both a strength and a weakness of the MillePede approach: the track propagation runs faster and provides an independent cross check of CMS's model, but can also introduce small inconsistencies with the final track reconstruction. In practice, large enough inconsistencies would lead to an incorrect alignment and would be caught during the validation procedure.

### 3.2.2  HipPy

The HipPy algorithm runs iteratively. In each iteration, it runs over the tracks, using as input the alignment derived in the previous iteration. Subsequently, it aligns each module individually, inverting a simple $6 \times 6$ (or $9 \times 9$, when the sensor curvature is also aligned) matrix for each module. In practice, when only small, random movements are involved, ten iterations are usually more than enough to deal with correlations between modules.

Figure 3.4 shows the capabilities of the HipPy algorithm. It can take input both from tracks ("AlCaReco") and from other sources of constraints, such as the optical survey or laser alignment system. The optical survey was in active use during Run 1 of the LHC. Although the laser system was decommissioned during Run 2, the functionality can be used to constrain degrees of freedom that tend to move in unphysical directions, such as the ones described in Sect. 3.4.1.1. Reading these

## HipPy - Hits and Impact Points algorithm Past Year-1 / Python
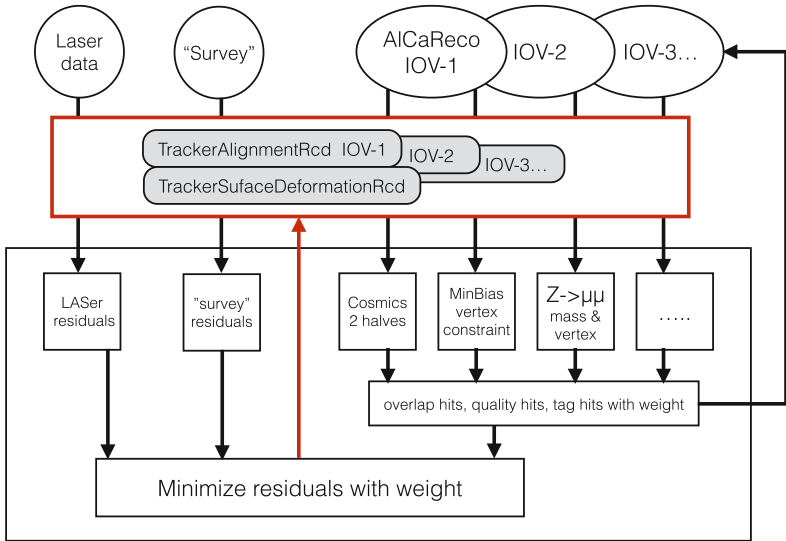


**Fig. 3.4**   Diagram describing the HipPy alignment procedure

sources of information, and processing them through the initial alignment for the iteration, HipPy calculates residuals, as shown in Fig. 3.2. Because HipPy's track reconstruction has access to the full CMS software, it has the capability to use any type of constraint defined in that software. Certain types of tracks and hits provide additional information—for example, the two tracks $Z \rightarrow \mu\mu$ decays can be constrained to come from the same vertex and to have a dimuon mass around 91.2 GeV, and cosmic rays provide a unique topology of tracks that can constrain degrees of freedom not covered well by collisions. These tracks can be weighted higher in the fit in order to best use this information.

In the end, the $\chi^2$ is minimized and the new output is created, which can include the modules' positions and rotations ("TrackerAlignmentRcd") and their curvatures ("TrackerSurfaceDeformationRcd"). Then, the next iteration is run, starting from the output of the previous iteration.

HipPy can also handle multi-IOV alignment, which is necessary when part of the detector shifts at certain points in time and we need to find a separate alignment for each time period, known as an "interval of validity" or IOV. The simplest way to handle this movement would be to simply derive a completely separate alignment for each IOV. However, if we assume that some degrees of freedom remained fixed in all IOVs, we can gain information by using *all* tracks to measure those degrees of freedom, while the other degrees of freedom are aligned separately for each IOV. In HipPy, this is handled by first aligning the components that frequently move, independently for each IOV. Subsequently, another alignment starts from the output of the first step and moves the individual components in a correlated way across all IOVs.

Typically, the large components of the pixel detector move most frequently and the strips move less often. An example alignment procedure might start by aligning the large pixel structures separately in each of 15 IOVs. After those outputs are collected, the pixel *modules* would be aligned within those structures for each of 5 IOVs, each of which spans 3 of the original 15 IOVs. In IOVs 1, 2, and 3, the large structures would be in 3 different places, but the relative positions and rotations of the modules within those structures would be common. Finally, the strip modules, which are known not to move frequently, would be aligned in a single alignment covering all 15 IOVs. The curvatures of all of the modules, which also do not change significantly with time, would also be aligned in the last step.

In dealing with a real systematic global movement, HipPy is slower to converge than MillePede, because the correlations between modules have to be solved through iteration. On the other hand, HipPy is more resilient than MillePede to *false* correlated movements.

## 3.3  Validation Procedures

Several validations are used to check the effect of alignments and determine whether a particular alignment performs well. A validation is essentially a projection of the alignment performance onto a particularly interesting degree of freedom. The quantities we choose to plot typically have a known value under perfectly aligned conditions. For example, a histogram of residuals is expected to peak at 0 with some width. The difference in parameters between two halves of a cosmic ray track is also expected to be 0 on average. The mass of a reconstructed $Z$ boson should be around 91.2 GeV. By detecting deviations from these expected values, especially deviations as a function of the track location or direction, we search for biases.

This section contains a description of several of the validation procedures used in alignment. Example plots can be found in Sects. 3.4 and 3.5.

### 3.3.1  Overlaps

The overlap validation monitors the alignment by using hits from tracks passing through regions where modules overlap within a layer of the tracker. In this method, the difference in residual values for the two measurements in the overlapping modules is calculated. Unexpected deviations between the reconstructed hits and the predicted positions can indicate a misalignment. This is characterized by a non-zero mean of the residuals. This method is particularly powerful because the distance between the overlapping modules from the same layer is relatively small, and therefore there is a relatively small uncertainty in track propagation through space between the modules. The double difference in estimated and measured hit positions becomes very sensitive to systematic deformations.
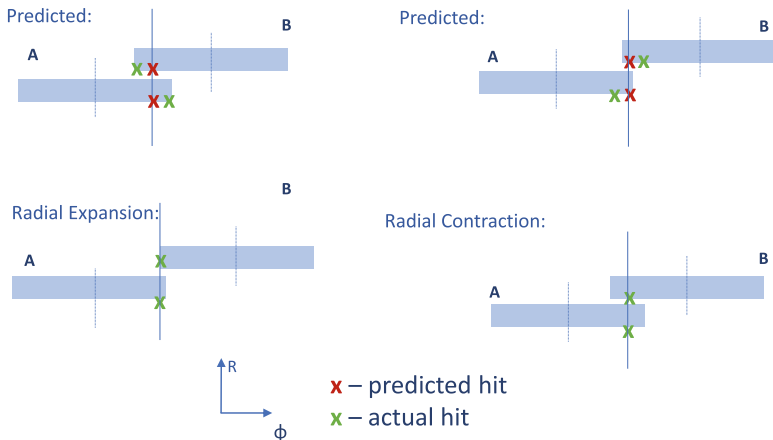
**Fig. 3.5** Illustration of the effect on overlaps between modules when they move relative to each other in the plane of the overlap. The top pictures show the module positions in the assumed geometry, with corresponding predicted hits in red. The bottom pictures show the actual positions of those modules, with the reconstructed hits in green. When projected onto the assumed geometry, the two hits are inconsistent, and the residuals have opposite signs between the two modules

Two effects in the overlap validation contribute to detecting misalignments. These effects are illustrated here for the radial misalignment, which will be discussed in detail in Sect. 3.4.5. The first effect, shown in Fig. 3.5, detects movement of the modules within the module plane, which is a second-order effect for the radial misalignment. This leads to a positive shift in residual mean for expansion and a negative shift for contraction, as shown in Fig. 3.5.

A second effect detects common movement of both modules perpendicular to themselves. The sensitivity to this movement comes from the fact that two nearby hits provide a precise measurement of the track angle, and the precision on this measurement, combined with knowledge of the track's momentum from the rest of the hits, can detect the change in track angle resulting from small perpendicular movements. This effect has an opposite effect for positively and negatively charged tracks because they curve in opposite directions in the magnetic field. Therefore, it does not affect the average overlap residual, but might be usable in future studies by isolating tracks of a particular charge. This effect is shown in Fig. 3.6.

### 3.3.2  Cosmic Track Splitting

Cosmic track splitting monitors the alignment of the tracker by independently reconstructing the upper and lower portions of cosmic ray tracks that go through the tracker. It then compares the parameters describing the two paths to see if they match up. This method is also powerful because we know that the two halves of a

**Fig. 3.6** Illustration of the effect on overlaps between modules when they move perpendicular to their plane. The bottom illustration shows the predicted position of the modules with predicted hits in red, while the top illustration shows their actual position with reconstructed hits in green. The radial expansion causes the modules to move along the track and, because of the curvature, to measure a different track angle
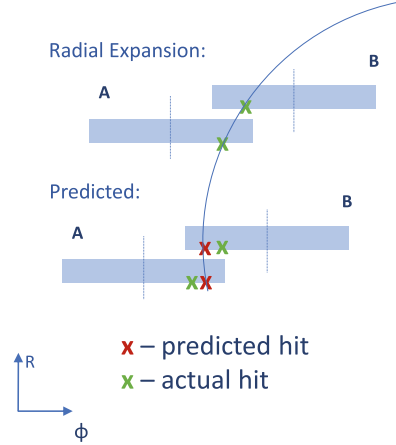


given cosmic track should have the same parameters at the origin, while each half of a track mimics a regular collision track originating from the interaction point. Systematic differences between the track halves can indicate a misalignment.

### 3.3.3 Z → μμ Decays

The Z → μμ validation uses a sample of Z → μμ events and looks for biases by reconstructing the mass of the muon pair. Each event, with its reconstructed mass, is placed into a bin depending on $\eta$ and $\phi$ of the muons. The mass distribution of each bin is then fit with a Gaussian, and the mean of this Gaussian is recorded as the reconstructed mass in that bin. The bins are then used to construct profiles of the mass as a function of $\eta$ or $\phi$. Misalignment in the tracker may be detected if the mean reconstructed mass strays from the expected value of 91.2 GeV, either uniformly or as a function of $\eta$ and $\phi$.

### 3.3.4 Distributions of the Medians of the Residuals (DMRs)

The distribution of the medians of the residuals (DMR) is a powerful tool to assess the statistical precision of alignment. While residuals themselves exhibit natural statistical fluctuations, the mean of those residuals should be zero in the limit of infinite statistics if there is no bias in the alignment and calibration of the detector. However, in order to reduce sensitivity to the tails of the distributions, the median is a better quantity to monitor compared to the mean. With a large enough number of tracks $N$ passing through each module, the median distribution should be centered at zero, and its width should scale as $1/\sqrt{N}$. With a large enough $N$, the width

of this distribution of the medians of residuals (DMR) is a measure of the local precision of the alignment results; deviations of the mean from zero indicate biases. The unbiased residuals are used in the DMR calculations, when each track is refitted using the alignment constants under consideration, and the hit prediction for each module is obtained from all other track hits. The median of the distribution of unbiased hit residuals is then taken for each module and histogrammed.

### 3.3.5   Primary Vertex Validation

The resolution of the reconstructed vertex position is driven by the pixel detector, since it is the closest detector to the interaction point and has the best hit resolution. The primary vertex residual method is based on the study of the distance between the track itself and the unbiased vertex, which is reconstructed without the track under scrutiny.

The distributions of the unbiased track-vertex residuals in the transverse plane, $d_{xy}$ and in the longitudinal direction, $d_z$, are studied in bins of track azimuth $\phi$ and pseudo-rapidity $\eta$. Random misalignments of the modules affect only the resolution of the unbiased track-vertex residual, increasing the width of the distributions, but without biasing their mean. Systematic movements of the modules will bias the distributions in a way that depends on the nature and size of the misalignment and of the selected tracks.

## 3.4   Systematic Misalignments

This section will discuss studies designed to detect systematic misalignments of the tracker, where all modules move in a correlated way. Two basic categories of systematic misalignments arise in alignment:

1. Weak modes are particular degrees of freedom that are difficult to detect using the standard alignment procedures. The most obvious, but not very interesting, example is a global movement of the whole detector: if we reconstructed tracks under the assumption that the entire CMS was transported to the moon, the shape and quality of all tracks would be unchanged. In this section, we study some more interesting cases. For example, a uniform radial expansion of the tracker by a factor $1 + \epsilon$ preserves the shape of tracks as helixes, but introduces biases in the track curvature and hence in the momentum.
2. Biases can also arise due to tension between conflicting constraints used in the alignment procedure. For example, sometimes alignment using cosmic rays and alignment using collisions will find two slightly different optimal positions, and in a real alignment, which uses both types of tracks, the algorithm tries to compromise between them. When this happens, it indicates a bias in

the procedure to reconstruct the tracks, before alignment enters the picture. The information provided by alignment can be used to improve the tracking procedure and, in the meantime, to find the best alignment to use for practical purposes given the non-optimal tracks. Applying weights to different kinds of tracks is a useful strategy in this case, because we can weight each track topology based on the confidence we have in the information provided by that topology.

The goal of this study was to identify systematic misalignments in CMS tracker geometry using various validation tools. The misalignments examined were first order misalignments of $\Delta\phi$, $\Delta r$ and $\Delta z$ as functions of $z$, $r$ and $\phi$. Each misalignment was characterized by some $\epsilon$. Systematic misalignments were generated on the ideal geometry using Monte Carlo. For each type of systematic misalignment, four different misalignments were generated using different values of $\epsilon$. The effect of each of the four misalignments was then found in some validation plot for each different systematic misalignment, and a fit was applied to determine the relationship between $\epsilon$ and a parameter of that fit.

We determined constraints on these systematic misalignments in the CMS Tracker by comparing the effects of misalignment in simulated Monte Carlo sample and in a representative Run2 data period using both collision and cosmic track data. The two most important validation techniques in this study are the overlap residuals and cosmic tracks split into two halves, have been the focus of this work, following on the original work during the tracker commissioning at the start of Run1 [2]. We have also revisited the systematic $z$-expansion in the TEC and TOB, following studies from the beginning of Run 2. Data from the 2017D run period, which ran from August 30 to September 20, 2017, was used with one of the intermediate alignments towards the final alignment to be used for reprocessing of the 2017 data. Values of $\epsilon$ for each systematic misalignment in this geometry were determined by looking at the parameter identified using the Monte Carlo simulation and using the corresponding fit to identify a characteristic $\epsilon$ according to Eq. (3.2).

Let us introduce nine first-order deformations natural for the cylindrical geometry of the CMS tracker and parameterize them with simple models described by a single parameter $\epsilon$. The misalignments in $\Delta z$, $\Delta r$, $\Delta\phi$ are functions of $z$, $r$, $\phi$, with an overall scaling given by $\epsilon$. The functional forms used to generate each systematic misalignment are listed in Table 3.1.

For each misalignment, we use the following equation to relate the systematic misalignment plots to $\epsilon$:

$$\text{Quantity from Plot} = a\epsilon + b \qquad (3.2)$$

where the quantity from a plot could be, for example, the mean of a distribution or a parameter extracted from a fit. In general, we expect $b = 0$, but we allow this additional degree of freedom in the equation to distinguish alignment issues from other possible effects related to reconstruction.

In describing the $\epsilon$ values for misalignments, care must be taken as to the sign. In order to save computing time, Monte Carlo simulations are always done

**Table 3.1** Table of the nine basic systematic distortions in the cylindrical system, with the names of each systematic misalignment, the function by which the misalignment is generated, and a validation type sensitive to the misalignment. In the formula for bowing, $z_0 = 271.846$ cm, which is the length of the tracker

|   | $\Delta z$ | $\Delta r$ | $\Delta \phi$ |
|---|---|---|---|
|   | **z-Expansion** | **Bowing** | **Twist** |
| $z$ | $\Delta z = \epsilon z$ | $\Delta r = \epsilon r(z_0^2 - z^2)$ | $\Delta \phi = \epsilon z$ |
|   | Overlap | Overlap | Z $\rightarrow \mu\mu$ |
|   | **Telescope** | **Radial** | **Layer rotation** |
| $r$ | $\Delta z = \epsilon r$ | $\Delta r = \epsilon r$ | $\Delta \phi = \epsilon r$ |
|   | Cosmics | Overlap | Cosmics |
|   | **Skew** | **Elliptical** | **Sagitta** |
| $\phi$ | $\Delta z = \epsilon \cos \phi$ | $\Delta r = \epsilon r \cos(2\phi)$ | $\Delta \phi = \epsilon \cos \phi$ |
|   | Cosmics | Cosmics | Cosmics |

using the ideal geometry, and the track reconstruction is done with a possibly misaligned geometry. That is, the "actual" detector position remains fixed to the ideal geometry, and the geometry used in reconstruction changes. When discussing data, the opposite convention is more natural: the geometry used in reconstruction is initially fixed and the actual detector moves.
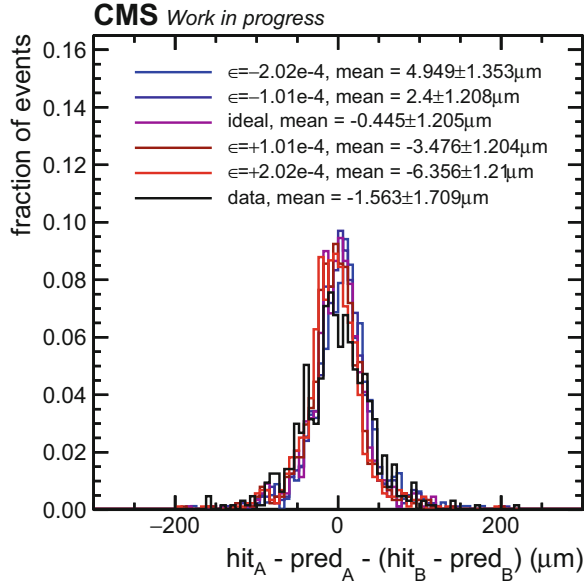
The equations in Table 3.1 are to the geometry used in reconstruction. Taking the radial misalignment as an example, a value of $\epsilon > 0$ means that the geometry used for reconstruction is expanded in the $r$ direction with respect to the geometry used in data taking. If this happens in data, we call it a radial contraction, because the detector has moved with respect to the expected position. This is the convention used in the text when describing the misalignments in data, as well as in Figs. 3.5 and 3.6 above.

### 3.4.1 z-Expansion

$z$-expansion (or contraction) is the uniform misalignment of the tracker in the $z$ direction as a function of $z$. Because the strip barrel modules are blind to the $z$ direction, this misalignment is difficult to detect there. $z$-expansion in BPIX can be detected using overlaps. We find that a change in $\epsilon$ causes a shift in the mean of the overlap validation plot for overlaps in the $z$ direction. The misalignment is an increasing function of $\epsilon$. The effect of the misalignment on the mean of the overlap plot is relatively small.

After fitting the mean of the Overlap Validation distribution in Fig. 3.7 with Eq. (3.2), we have that $a = (-2.83 \pm 0.05) \times 10^4$ μm and $b = (0.58 \pm 0.07)$ μm. We find that in the pixels, the run 2017D $\epsilon$ corresponding to $z$-expansion is $(3 \pm 6) \times 10^{-5}$. In BPIX (at $z = 260$ mm), this corresponds to a contraction of $(9 \pm 16)$ μm, consistent with zero.

**Fig. 3.7** $z$-expansion validation: distribution of overlaps in the $z$ direction with modules overlapping in the $z$ direction in BPIX for cosmic muon events in Monte Carlo and data. The Monte Carlo events are simulated with the ideal detector geometry and reconstructed using five geometries, corresponding to the $z$-expansion misalignment with $\epsilon = -2.02 \times 10^{-4}$, $-1.01 \times 10^{-4}$, $0$, $1.01 \times 10^{-4}$, and $2.02 \times 10^{-4}$

**CMS** *Work in progress*

— $\epsilon$=−2.02e-4, mean = 4.949±1.353μm
— $\epsilon$=−1.01e-4, mean = 2.4±1.208μm
— ideal, mean = -0.445±1.205μm
— $\epsilon$=+1.01e-4, mean = -3.476±1.204μm
— $\epsilon$=+2.02e-4, mean = -6.356±1.21μm
— data, mean = -1.563±1.709μm

fraction of events

$\text{hit}_A - \text{pred}_A - (\text{hit}_B - \text{pred}_B)$ (μm)

### 3.4.1.1   $z$-Expansion in the TEC: DMRs Separated by Charge

In previous alignments, it has been noticed that TEC has experienced some $z$-expansion. This is caused by a tension between collisions and cosmics, as the collisions appear to show a $z$-expansion but the cosmics do not. It was also found that in TEC with collision data generated by Monte Carlo, there was a bias between positively and negatively charged tracks, as shown in Fig. 3.8, indicating that there may also be a tension between positive and negative tracks in alignment. A possible explanation could be biased modeling of the track propagation, possibly due to the material model. This suggestion is supported by the fact that the bias is reduced for higher-momentum tracks. Since the same effect appears in both data and MC, it should be possible to track it further with MC simulation. Whatever the source of this effect, it comes from outside alignment, and further study is beyond the scope of this work.

## 3.4.2   Bowing

Bowing is the misalignment of the tracker in the $r$ direction as a function of $z$. It is similar to the radial expansion, which will be discussed in Sect. 3.4.5, and differs only by the fact that the bowing effect is a function of $z$. For small values of $\epsilon$, many millions of events would be needed to measure the $z$ modulation. However, fewer events are needed to *exclude* the presence of either a bowing or a radial misalign-

**Fig. 3.8**  *z*-expansion
validation in the TEC: DMR
separated by charge for
cosmics and collisions in
Monte Carlo. These events
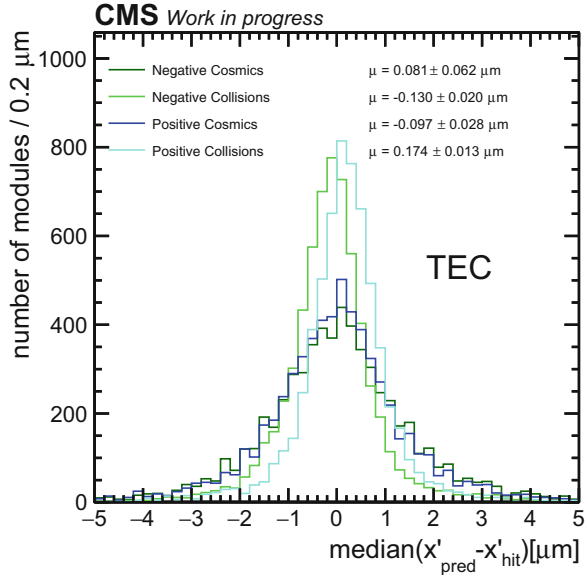are simulated with the ideal
detector geometry



**Fig. 3.9**  Bowing validation:
distribution of overlaps in the
$\phi$ direction with modules
overlapping in the $\phi$ direction
in TOB for cosmic muon
tracks in Monte Carlo and
data. The Monte Carlo events
are simulated with the ideal
detector geometry and
reconstructed using five
geometries, corresponding to
the Bowing misalignment
with $\epsilon = 6.77 \times 10^{-9}$ cm$^2$,
$3.385 \times 10^{-9}$ cm$^2$, 0,
$-3.385 \times 10^{-9}$ cm$^2$, and
$-6.77 \times 10^{-9}$ cm$^2$
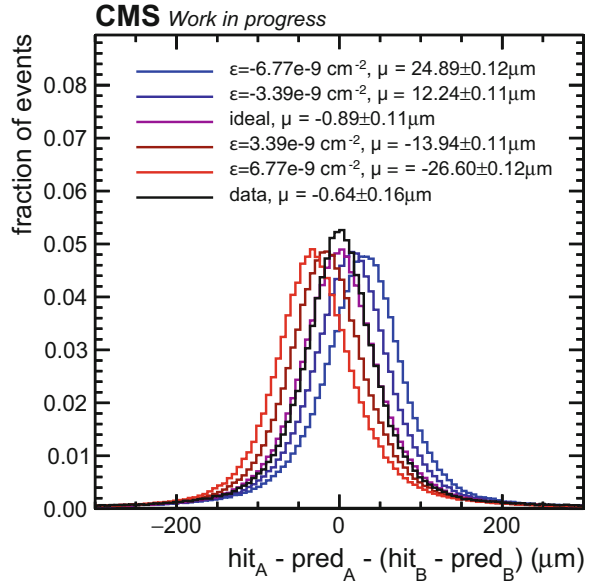


ment. There is a clear relationship between $\epsilon$ set and the mean value of the overlap
distribution, $\mu = \epsilon(-3.816 \pm 0.014) \times 10^9$ $\mu$m cm$^2$ + $(-0.86 \pm 0.05)$ $\mu$m. In data,
we observe $\mu = (-0.64 \pm 0.16)$ $\mu$m, yielding $\epsilon = (-5.8 \pm 4.5) \times 10^{-11}$ cm$^2$. See
Fig. 3.9 for results.

**Fig. 3.10** Twist validation: profile of $M_{\mu\mu}$ vs. $\Delta\eta$ for $Z \to \mu\mu$ events in Monte Carlo and data. The Monte Carlo events are simulated with the ideal detector geometry and reconstructed using five geometries, corresponding to the Twist misalignment with $\epsilon = 2.04 \times 10^{-6}\,\mathrm{cm}^{-1}$, $1.02 \times 10^{-6}\,\mathrm{cm}^{-1}$, 0, $-1.02 \times 10^{-6}\,\mathrm{cm}^{-1}$, and $-2.04 \times 10^{-6}\,\mathrm{cm}^{-1}$
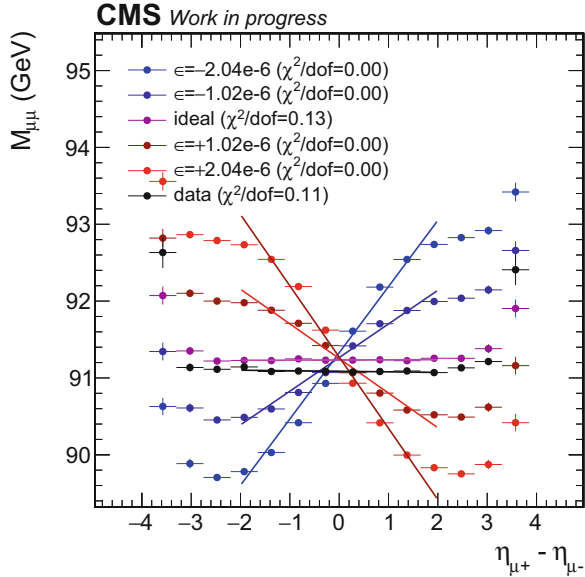
### 3.4.3 Twist

Twist is the misalignment of the tracker in the $\phi$ direction as a function of $z$. As such, twist shows up clearly in $Z \to \mu\mu$ plots, and also in overlap plots. The parameter used is the slope of the $M_{\mu\mu}$ vs. $\Delta\eta$ plot, taken from $\Delta\eta = -2$ to $+2$, as the plot becomes nonlinear for larger $\Delta\eta$. Fitting to the Monte Carlo events, we find that $a = (-4.42 \pm 0.05) \times 10^{-5}$ GeV cm and $b = (-0.018 \pm 0.008)$ GeV. The slope in data was found to be $(-7 \pm 4) \times 10^{-3}$ GeV, corresponding to $\epsilon = (-2.5 \pm 2.2) \times 10^{-8}\,\mathrm{cm}^{-1}$. See Fig. 3.10 for results.

### 3.4.4 Telescope

Telescope is the uniform misalignment of the tracker in the $\Delta z$ direction as a function of $r$ ($z \to z + \epsilon r$). This creates concentric rings that are offset in the $z$-direction, and this misalignment can be visualized by imagining an actual telescope. Because of its $z$-dependence, Telescope is identified primarily with the track reconstruction of cosmic rays. From fitting Monte Carlo data, we find $a = 3508 \pm 40$ and $b = -0.86 \pm 0.06$. Running this validation on observed data and plugging the mean into Eq. (3.2) yields $\epsilon = (-2.2 \pm 0.5) \times 10^{-5}$. In the pixel detector ($r = 160$ mm) this epsilon corresponds to a maximum relative movement of 3.5 μm, and in the whole tracker ($r = 1100$ mm) it corresponds to a maximum movement of 24 μm. See Fig. 3.11 for results.

**Fig. 3.11** Telescope
validation: distribution of
$\Delta\theta/\delta(\Delta\theta)$ for cosmic muons
in Monte Carlo and data. The
Monte Carlo events are
simulated with the ideal
detector geometry and
reconstructed using five
geometries, corresponding to
the Telescope misalignment
with $\epsilon = 5 \times 10^{-4}$,
$2.5 \times 10^{-4}, 0, -2.5 \times 10^{-4}$,
and $-5 \times 10^{-4}$
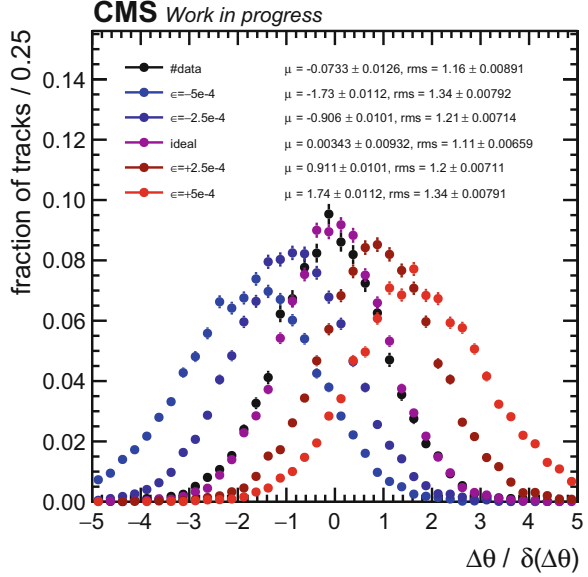


### 3.4.5   Radial

Radial is the uniform misalignment of the tracker in the $\Delta r$ direction as a function
of $r$ $(r \rightarrow r + \epsilon r)$. Because of the uniform and symmetric nature of this
misalignment, it is not easily detected with cosmic track-splitting or $Z \rightarrow \mu\mu$
decays. However, it is easily detected using the Overlap Validation since, in the
case of a radial expansion, modules that overlap in the radial direction will move
uniformly apart. Therefore, the difference between actual and predicted hit location
on two overlapping modules is a good indicator of a radial expansion or contraction.
In fact, the linear relationship between the mean of the Overlap Validation plots and
the magnitude of the radial misalignment can be used to categorize the presence of
radial expansion or contraction in real tracker data.

In TOB, after running the Overlap Validation on Monte Carlo data and fitting
the results with Eq. (3.2), we find $a = (-7.461 \pm 0.010) \times 10^4\,\mu$m and $b =
(-6.023 \pm 0.034)\,\mu$m. After applying a similar method to tracker data and plugging
the mean from the overlap validation into the fit, $\epsilon = (2.23 \pm 0.40) \times 10^{-5}$.

In TIB, we find $a = (-5.035 \pm 0.010) \times 10^4\,\mu$m, $b = (-3.460 \pm 0.033)\,\mu$m,
and $\epsilon = (-2.82 \pm 0.34) \times 10^{-5}$.

In BPIX, we find $a=(-1.4012 \pm 0.0008) \times 10^4\,\mu$m, $b=(-1.6450 \pm 0.0030)\,\mu$m,
and $\epsilon = (-9.26 \pm 0.39) \times 10^{-5}$.

Based on the relative epsilon values, we measure a greater radial bias in BPIX
than in the other subdetectors. The radius of BPIX is approximately 160 mm, so this
corresponds to an overall radial expansion of approximately 15 μm. In TIB ($r =
550$ mm), we find a *contraction* of 15 μm, and in TOB ($r = 1100$ mm), we find a
*contraction* of 24 μm. See Fig. 3.12 for results.
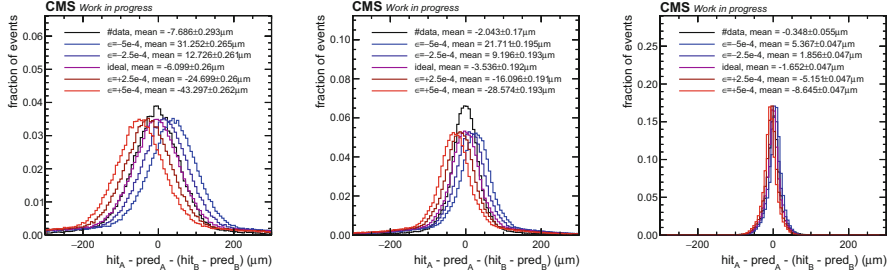
**Fig. 3.12** Radial expansion validation: distribution of overlaps in the $\phi$ direction for modules in the $\phi$ direction in TOB, TIB, and BPIX for collision events in Monte Carlo and data. The Monte Carlo events are simulated with the ideal detector geometry and reconstructed using five geometries, corresponding to the radial misalignment with $\epsilon = 5 \times 10^{-4}$, $2.5 \times 10^{-4}$, $0$, $-2.5 \times 10^{-4}$, and $-5 \times 10^{-4}$

**Fig. 3.13** Layer rotation validation: distribution of $\Delta(q/p_t)$ for cosmic muon events in Monte Carlo and data. The Monte Carlo events are simulated with the ideal detector geometry and reconstructed using five geometries, corresponding to the Layer Rotation misalignment with $\epsilon = 9.43 \times 10^{-6}\,\mathrm{cm}^{-1}$, $4.715 \times 10^{-6}\,\mathrm{cm}^{-1}$, $0$, $-4.715 \times 10^{-6}\,\mathrm{cm}^{-1}$, and $-9.43 \times 10^{-6}\,\mathrm{cm}^{-1}$
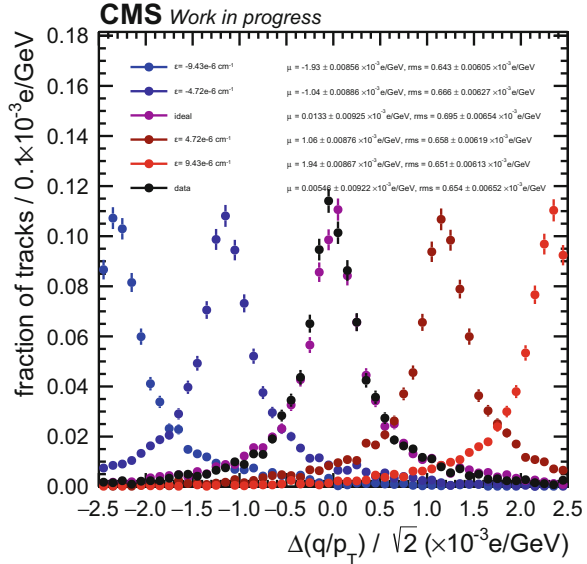


### 3.4.6 Layer Rotation

Layer rotation is the misalignment of the tracker in the $\phi$ direction as a function of $r$. The outer layers twist in one direction, while the inner layers twist in the other direction. The distortion is easily picked up with cosmic track-splitting, as we can see a change in track curvature between the two tracks. As such, we take the mean of a value proportional to the curvature, for each epsilon. We found a linear relationship between $\mu$ and $\epsilon$, using Eq. (3.2), with $a = (208.5 \pm 3.9)$ cm e/GeV and $b = (0.9 \pm 2.6) \times 10^{-5}$ e/GeV. For the data, $\mu = (0.005 \pm 0.009)$ e/GeV, so $\epsilon = (-0.2 \pm 1.4) \times 10^{-7}\,\mathrm{cm}^{-1}$ See Fig. 3.13 for results.

**Fig. 3.14** Skew validation:
Profile of $\Delta d_z / \sqrt{2}$ vs $\phi$ for
cosmic muon events in Monte
Carlo and data. The Monte
Carlo events are simulated
with the ideal detector
geometry and reconstructed
using five geometries,
corresponding to the Skew
misalignment with
$\epsilon = 5.5 \times 10^{-2}$ cm,
$2.25 \times 10^{-2}$ cm, 0,
$-2.25 \times 10^{-2}$ cm, and
$-5.5 \times 10^{-2}$ cm
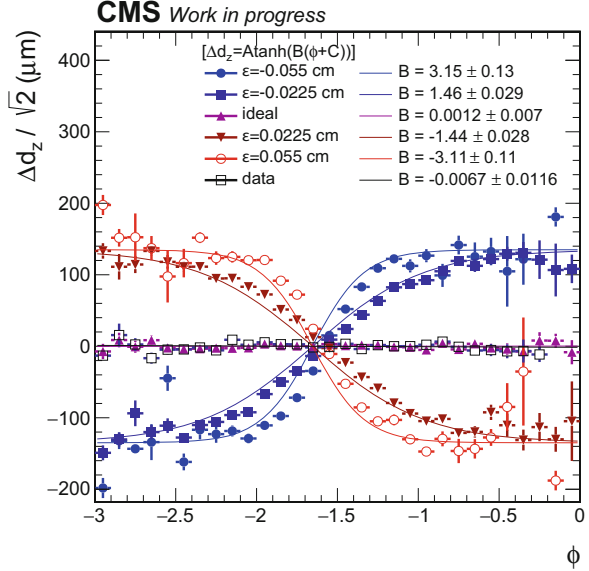


## 3.4.7   Skew

Skew is the misalignment of the tracker in the $z$ direction as a function of $\phi$.
Because of the $\phi$ dependency, it can be detected with cosmic track splitting. We
found that the plots of $\Delta d_z$ vs. $\phi$ which could be fit by a hyperbolic tangent function
$A \times \tanh(B(\phi+C))$, which can give us $\epsilon$. Setting $A = 134$ and $C = 1.654$, we found
a linear relationship between $B$ and $\epsilon$ using Eq. (3.2), with $a = (-62.5 \pm 1.9)$ cm
and $b = (0.002 \pm 0.016)$ cm. Since for the data, $B = -0.007 \pm 0.012$, $\epsilon = (1.4 \pm 3.2) \times 10^{-4}$ cm. See Fig. 3.14 for results.

## 3.4.8   Elliptical

Elliptical is the uniform misalignment of the tracker in the $\Delta r$ direction as a function
of $\phi (r \rightarrow r + r\epsilon \cos(2\phi + \delta))$. Because of its $\phi$ dependency, elliptical is easily
detected with cosmic track-splitting. This misalignment is especially clear in the
modulation of the difference in the impact parameter $\Delta d_{xy}$ as a function of the
track's angle $\phi$. We fit this modulation to a sine function, $\Delta d_{xy} = -A \times \sin(2\phi)$,
and find a linear relationship between $A$ and $\epsilon$. Using Eq. (3.2), we find $a = (8.63 \pm 0.11) \times 10^4$ μm and $b = (-0.22 \pm 0.34)$ μm. Using Eq. (3.2), this yields
$\epsilon = 2.5 \pm 0.6 \times 10^{-5}$. In the pixel detector ($r = 160$ mm), this $\epsilon$ corresponds
to a maximum movement of 4 μm, and in the whole tracker ($r = 1100$ mm) it
corresponds to a maximum movement of 30 μm. The positive sign of $\epsilon$ means that

**Fig. 3.15** Elliptical validation: profile of $\Delta d_{xy}/\sqrt{2}$ vs. $\phi$ for cosmic muon events in Monte Carlo and data. The Monte Carlo events are simulated with the ideal detector geometry and reconstructed using five geometries, corresponding to the elliptical misalignment with $\epsilon = 5 \times 10^{-4}$, $2.5 \times 10^{-4}$, $0$, $-2.5 \times 10^{-4}$, and $-5 \times 10^{-4}$
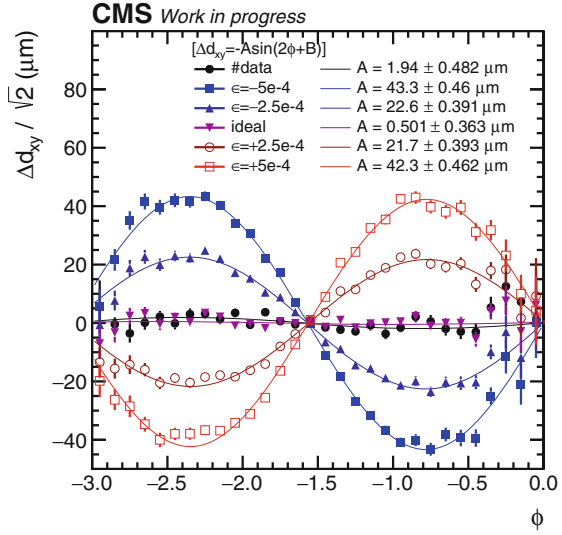


there is a expansion in $\Delta r$ as a function of $\phi$, with the long axis of the resulting oval shape is in the $y$ direction. See Fig. 3.15 for results.

### 3.4.9 Sagitta

Sagitta is the uniform misalignment of the tracker in the $\Delta\phi$ direction as a function of $\phi$. As with the elliptical misalignment, the $\phi$ dependence in sagitta allows it to be detected with the cosmic track-splitting validation. The effect of the misalignment can be seen in plots with $\Delta\phi$ vs $\phi$. Figure 3.16 shows sinusoidal distributions, fit to $-A \times \cos(\phi + B)$, We fit to Eq. (3.2) using the amplitude ($A$) of the sine wave as the quantity from the plot. Fitting to Monte Carlo, we find that $a = 1199 \pm 5$ and $b = (-2 \pm 2) \times 10^{-3}$. For data, we find that $A = (0.052 \pm 0.009)\,\mu m$ and thus $\epsilon = (4.5 \pm 0.7) \times 10^{-5}$ mrad. See Fig. 3.16 for results.

### 3.4.10 Summary

In this section, we have introduced nine first-order deformations of the CMS tracker geometry natural for the cylindrical geometry and parameterized them with the simple models described by a single parameter $\epsilon$. We have determined constraints on these systematic misalignments by examining the effects of misalignment in simulated Monte Carlo sample, and then comparing to collision and cosmic track data from Run2. A characteristic $\epsilon$ value, describing the magnitude of a

**Fig. 3.16** Sagitta validation: distribution of $\Delta\phi$ vs. $\phi$ for cosmic muon events in Monte Carlo and data. The Monte Carlo events are simulated with the ideal detector geometry and reconstructed using five geometries, corresponding to the Sagitta misalignment with $\epsilon = 5 \times 10^{-4}$, $2.5 \times 10^{-4}$, $0$, $-2.5 \times 10^{-4}$, and $-5 \times 10^{-4}$
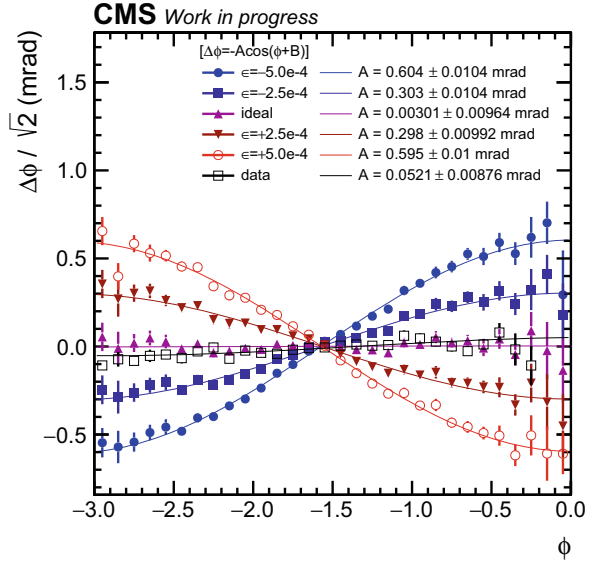


misalignment in each of the nine scenarios, has been determined for each of the systematic misalignments, along with a corresponding upper limit on the magnitude of $\epsilon$. These results are summarized in Table 3.2. The constraints are presented at 68% CL ($1\sigma$). The obtained constraints could be used in physics analyses sensitive to systematic distortions in the tracker geometry to set limits on possible biases.

It may be possible that there is a systematic misalignment present in the tracker that is not represented by any of the nine misalignments studied in this note. However, such a misalignment would likely be a higher order function of z, r or $\phi$ than the ones used in this study and would likely still have some first order component that would appear in the validation plots described in this note. It would still be useful to examine such systematic misalignments to better characterize the systematic misalignments in the tracker.

One indication of a higher order systematic misalignment would be potential differences between different kinds of tracks or different kinds of plots in estimating the magnitude of the same misalignment. These differences could indicate that the misalignment is not exactly of the form studied or could indicate biases in track reconstruction, unrelated to alignment, similar to the ones seen in Sect. 3.4.1.1.

While we do not pursue this in detail in this study, in the case of radial expansion (Sect. 3.4.5) we obtained three different estimates of $\epsilon$, one each in BPIX, TIB, and TOB, and found different $\epsilon$ values, so the misalignment appears to be a higher order function of $r$. Additionally, because bowing and radial are so similar, we can compare our estimate of $\epsilon$ for bowing in TOB, obtained using cosmic rays, and our estimate of $\epsilon$ for radial in TOB, obtained using collision tracks. In the center plane of the detector, where bowing's effect is largest, a bowing misalignment with $\epsilon_b = \epsilon$ is equivalent to a radial misalignment with $\epsilon_r = \epsilon_b z_0^2$. Using $z_0 = 271.846$ cm and

**Table 3.2** Summary table of $\epsilon$ in each misalignment, each misalignment is listed with its corresponding validation type and a maximum amplitude of $\epsilon$ (at 68% CL, or $1\sigma$)

| | $\Delta z$ | $\Delta r$ | $\Delta \phi$ |
|---|---|---|---|
| $z$ | **$z$-Expansion** $\Delta z = \epsilon z$ Overlap $\epsilon = (3 \pm 6) \times 10^{-5}$ $\lvert \epsilon \rvert < 9 \times 10^{5}$ | **Bowing** $\Delta r = \epsilon r (z_0^2 - z^2)$ Overlap $\epsilon = (-5.8 \pm 4.5) \times 10^{-11}$ cm$^{-2}$ $\lvert \epsilon \rvert < 1.0 \times 10^{-10}$ cm$^{-2}$ | **Twist** $\Delta \phi = \epsilon z$ $Z \to \mu\mu$ $\epsilon = (-2.5 \pm 2.2) \times 10^{-8}$ cm$^{-1}$ $\lvert \epsilon \rvert < 4.7 \times 10^{-8}$ cm$^{-1}$ |
| $r$ | **Telescope** $\Delta z = \epsilon r$ Cosmics $\epsilon = (2.18 \pm 0.48) \times 10^{-5}$ $\lvert \epsilon \rvert < 2.7 \times 10^{5}$ | **Radial** $\Delta r = \epsilon r$ Overlap $\epsilon = (-9.26 \pm 0.39) \times 10^{-5}$ $\lvert \epsilon \rvert < 9.9 \times 10^{5}$ | **Layer rotation** $\Delta \phi = \epsilon r$ Cosmics $\epsilon = (-0.2 \pm 1.4) \times 10^{-7}$ cm$^{-1}$ $\lvert \epsilon \rvert < 1.6 \times 10^{-7}$ cm$^{-1}$ |
| $\phi$ | **Skew** $\Delta z = \epsilon \cos \phi$ Cosmics $\epsilon = (1.4 \pm 3.2) \times 10^{-4}$ cm $\lvert \epsilon \rvert < 4.6 \times 10^{-4}$ cm | **Elliptical** $\Delta r = \epsilon r \cos(2\phi)$ Cosmics $\epsilon = (2.5 \pm 0.6) \times 10^{-5}$ $\lvert \epsilon \rvert < 3.1 \times 10^{5}$ | **Sagitta** $\Delta \phi = \epsilon \cos \phi$ Cosmics $\epsilon = (4.5 \pm 0.7) \times 10^{-5}$ $\lvert \epsilon \rvert < 5.2 \times 10^{5}$ |

our measured value for $\epsilon_b$, we find $\epsilon_r = (-4.2 \pm 3.6) \times 10^{-6}$, which is $2\sigma$ away from our direct estimate using collision tracks, $\epsilon_r = \epsilon = (2.23 \pm 0.40) \times 10^{-5}$. This may indicate that the misalignment has some other position dependence that affects cosmic rays differently from collisions, though to make a more definite statement it would be necessary to run over more events.

It is interesting to note that four systematic misalignments were found with $\epsilon$ inconsistent with zero at very high confidence level: Telescope, Radial, Elliptical, and Sagitta. This may indicate either some time-dependence in the systematic distortions within a given IOV, or more likely some tension between different constraints in the alignment procedure. The observed effects are still small and would not affect most of the physics analyses on CMS, but further investigation of these effects will be a natural continuation of these studies for further refinement of the alignment procedure.

## 3.5  Performance During Run II of the LHC

This section will cover some of the alignment results throughout Run 2, which ran from 2015–2018. In each year, a selection of plots are shown, so that each type of validation is covered between the 4 years. For comprehensive plots for each year, see [6–9].
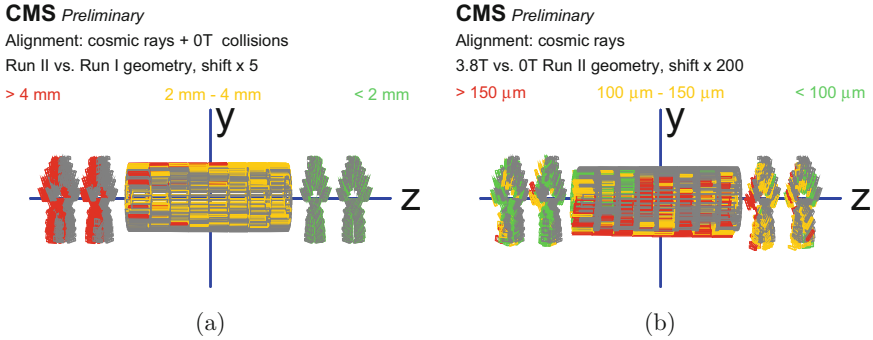
**Fig. 3.17** Illustration of the differences in the pixel detector position (**a**) between the end of Run 1 of the LHC and the beginning of Run 2, and (**b**) between the cosmic ray data collection with the magnetic field turned off and with the field turned on. In both plots, the older module positions are shown in gray and the new positions are shown in brighter colors. the colors indicate which modules moved the most, but the color scaling is different between the plots to better illustrate the scale of the movements [6]

### 3.5.1  2015 Startup

The 2015 run of the LHC saw the first collisions at 13 TeV. It was primarily a preparation run, with only 2.7 fb$^{-1}$ of collisions. During the long shutdown since Run 1, the detector had been opened and the pixel detector was completely removed and replaced, so large movements were expected. Figure 3.17a shows the differences in the pixel detector between the end of Run 1 and the beginning of Run 2. The larger movements are seen in the $-z$ forward pixel detector, which was inserted a few millimeters away from its previous position. The alignment result was the first indication that this had happened. BPIX is mostly yellow in this plot due to a recentering procedure that was performed. Figure 3.17b shows the much smaller movements that resulted from turning on the magnetic field.

### 3.5.2  2016

The 2016 run produced the first higher luminosity 13 TeV proton collisions. As one of the 3 years of Run 2 designed for precise physics analyses, it was important to maintain the performance throughout the year. Figure 3.18 shows primary vertex validation plots for the 2016 data, comparing the performance before and after the alignment was performed.
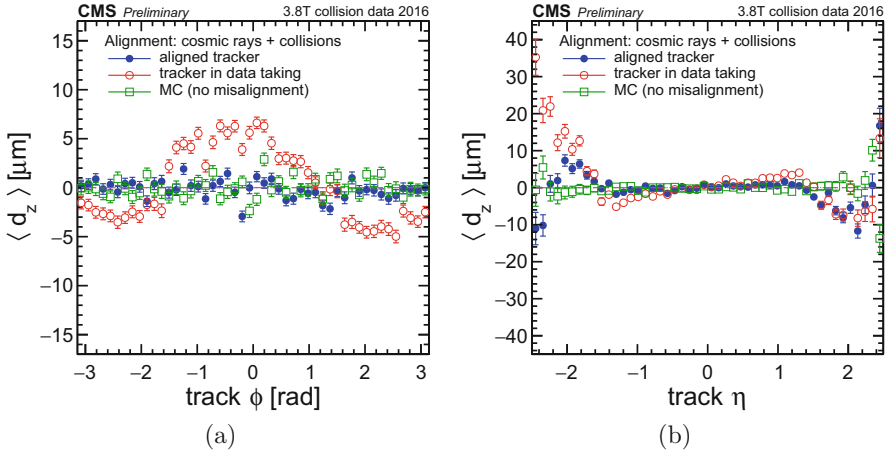
**Fig. 3.18** Primary vertex validation plots for 2016 data, comparing the initial alignment used for data taking in red, the alignment used to rereconstruct the data for data analyses in blue, and the Monte Carlo simulation reconstructed under ideal conditions in green. The $z$ distance between the probe track and the vertex is plotted as a function of (**a**) $\phi$ and (**b**) $\eta$ of the probe track [7]

### 3.5.3   2017

For the 2017 run, an entirely new pixel detector was installed. This detector was designed to provide better resolution for tracks by adding an additional BPIX layer closer to the beam pipe and an additional disk on each side of FPIX. At the beginning of 2017, this detector had to be aligned from scratch. The DMR plots in Fig. 3.19 show the improvement resulting from the alignment, first using cosmic rays and then using the first collisions. The plot in Fig. 3.20 shows the effect of the alignment on $\phi$ modulation of the reconstructed Z boson mass. This kind of modulation is characteristic of a weak mode effect, described in Sect. 3.4, and is fixed by the alignment.

### 3.5.4   2018

Figure 3.21 shows a comparison of track splitting performance on 2018 cosmic ray data between the alignment at the end of 2017 and at the beginning of 2018.
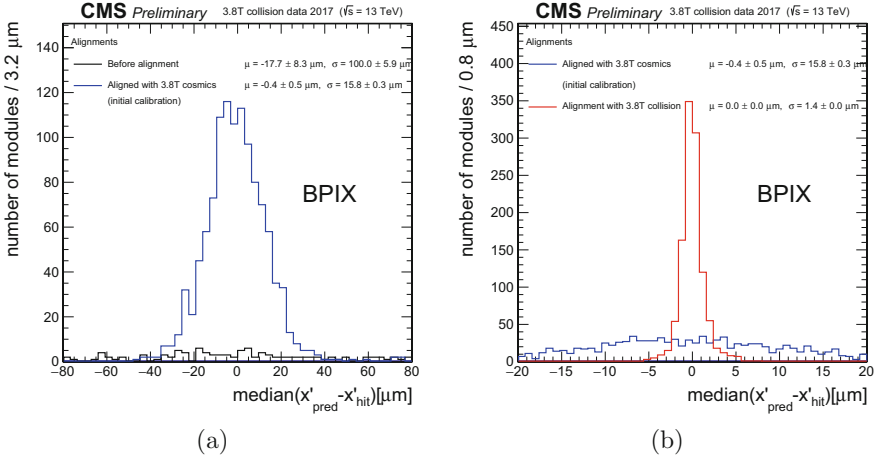
(a)                                                              (b)

**Fig. 3.19** DMR plots for 2017 collision data, comparing three different alignments: the initial geometry used for data taking (black), the first calibration of the detector using cosmic rays (blue), and the updated alignment derived using collision data (red). The alignment with cosmic rays significantly improves the performance, and the alignment with collisions, sensitive to different degrees of freedom that are relevant to the collision tracks used in the validation, brings further improvements [8]

**Fig. 3.20** A $Z \to \mu\mu$ validation plot for 2017, plotting the average reconstructed mass of the dimuon system as a function of $\phi$ of the positively charged muon [8]
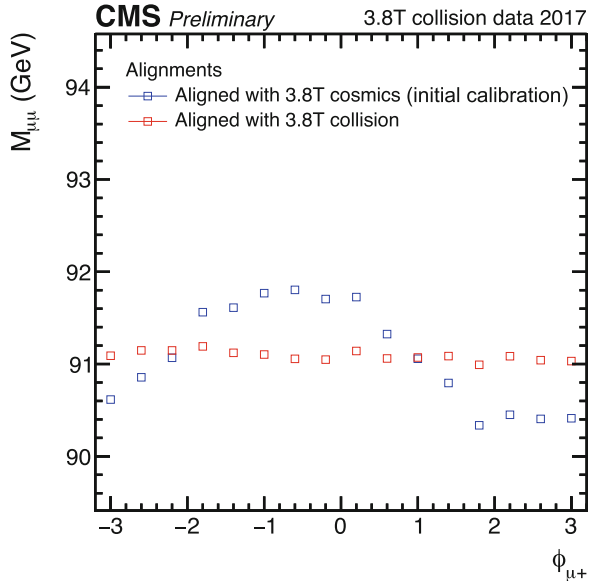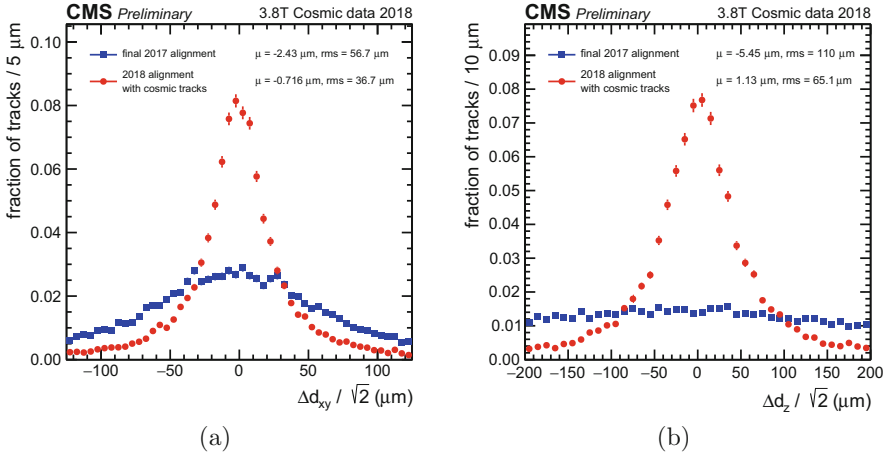
**Fig. 3.21** Track splitting plots, showing histograms of $\Delta d_{xy}$ and $\Delta d_z$ for the 2018 alignment, reconstructed with the alignment from the end of 2017 and the alignment derived in 2018 [9]

## 3.6  Conclusions and Outlook

The results shown here are just a small selection of the plots produced by the CMS tracker alignment group over Run 2 of the LHC. The detector conditions changed from what they were in Run 1, first with the increased collision energy in 2015 and subsequently with the new pixel detector in 2017. The conditions will become even more challenging at the High Luminosity LHC (HL-LHC), when the luminosity delivered by the LHC, and hence the number of simultaneous collisions, will increase drastically. The plan is to upgrade the tracker again at that time, including a much more extensive forward pixel detector that can handle the large numbers of particles produced close to the beam line, and the forward degrees of freedom are among the most difficult to align.

Extensive studies are ongoing and will continue throughout Run 3 in order to prepare for these conditions, which will be more challenging than any faced so far. The alignment group and procedures have proven to be flexible and resilient to date, and should be able to incorporate the new developments needed to deliver fast and precise alignments throughout the run period of the HL-LHC.

## References

1. W. Adam et al., Alignment of the CMS silicon strip tracker during standalone commissioning. J. Instrum. **4**, T07001 (2009). https://doi.org/10.1088/1748-0221/4/07/T07001. arXiv: 0904.1220 [physics.ins-det]
2. S. Chatrchyan et al., Alignment of the CMS silicon tracker during commissioning with cosmic rays. J. Instrum. **5**, T03009 (2010). https://doi.org/10.1088/1748-0221/5/03/T03009. arXiv: 0910.2505 [physics.ins-det]

3. S. Chatrchyan et al., Alignment of the CMS tracker with LHC and cosmic ray data. J. Instrum. **9**, P06009 (2014). https://doi.org/10.1088/1748-0221/9/06/P06009. arXiv: 1403.2286 [physics.ins-det]
4. V. Blobel, C. Kleinwort, A New method for the high precision alignment of track detectors, in *Advanced Statistical Techniques in Particle Physics. Proceedings, Conference, Durham, UK, March 18-22, 2002* (2002). arXiv: hep-ex/0208021 [hep-ex]. http://www.ippp.dur.ac.uk/Workshops/02/statistics/proceedings//blobel1.pdf
5. G. Flucke, P. Schleper, G. Steinbruck, M. Stoye, CMS silicon tracker alignment strategy with the Millepede II algorithm. J. Instrum. **3**, P09002 (2008). https://doi.org/10.1088/1748-0221/3/09/P09002
6. CMS Collaboration, Alignment of the CMS tracking-detector with first 2015 cosmic-ray and collision data. (2015). http://cds.cern.ch/record/2041841
7. CMS Collaboration, CMS tracker alignment performance results 2016 (2017). http://cds.cern.ch/record/2273267
8. CMS Collaboration, Tracker alignment performance plots after commissioning (2017). http://cds.cern.ch/record/2297526
9. CMS Collaboration, CMS tracker alignment performance results 2018 (2018). https://cds.cern.ch/record/2650977